A 3D time domain numerical model based on half-space Green's function for soil-structure interaction analysis.

P. Galvín · **J. Maestre** · **A. Romero**

Abstract This paper presents a numerical method based on a three dimensional boundary element-finite element (BEM-FEM) coupled formulation in the time domain. The proposed model allows studying soil-structure interaction problems. The soil is modelled with the BEM, where the radiation condition is implicitly satisfied in the fundamental solution. Half-space Green's function including internal soil damping is considered as the fundamental solution. An effective treatment based on the integration into a complex Jordan path is proposed to avoid the singularities at the arrival time of the Rayleigh waves. The efficiency of the BEM is improved taking into account the spatial symmetry and the invariance of the fundamental solution when it is expressed in a dimensionless form. The FEM is used to represent the structure. The proposed method is validated by comparison with analytical solutions and numerical results presented in the literature. Finally, a soil-structure interaction problem concerning with a building subjected to different incident wave fields is studied.

Keywords Half-space fundamental solution · Internal soil damping · BEM-FEM coupling · Soil-structure interaction · Time domain

1 Introduction

Soil-Structure Interaction (SSI) is a field of interest that involves structural analysis considering flexibility and damping due to the soil. Induced vibrations by rotatory machines, dynamic effects due to railway and road traffic, seismic problems, and dynamic behaviour of foundation systems are examples where SSI is an important issue. The effects of SSI are important and cannot be neglected in this type of problems [28]. Kausel [15] presented an exhaustive review of the main developments in this topic. Recently, Clouteau et al. [6] also reviewed different proposed numerical models to study the dynamic behaviour of structures on elastic media.

Escuela Técnica Superior de Ingeniería,
Universidad de Sevilla, Camino de los Descubrimientos, 41092 Sevilla, Spain
Tel.: +34 955487293 (94)
Fax: +34 954487296
E-mail: pedrogalvin@us.es

Numerical models based on the Boundary Element Method (BEM) and the Finite Element Method (FEM) allow to study SSI problems rigorously. The BEM [8] is especially suited for the analysis of wave propagation in soils. Sommerfeld radiation condition [9] is satisfied implicitly and its semi-infinite character is well considered. The FEM is very useful to analyse the dynamic behaviour of structures accounting for nonlinear effects [29].

BEM models in time domain are usually based on full-space fundamental solutions due to their simplicity. Among other authors, Rizos and Karabalis [23] presented a BEM model to study general elastodynamic problems using the solution to Stokes' problem within B-Spline polynomials. Schanz [26] proposed a BEM formulation based on a fundamental solution in the Laplace domain which is transformed at each time step using the convolution quadrature method. Araújo et al. [1] developed a BEM model based on the time-marching Wilson θ-method. Marrero and Domínguez [18] presented a BEM formulation for the solution of transient problems in bounded domains using an explicit full-space fundamental solution [9]. Later, Galvín and Domínguez [10] extended this model to study wave propagation in unbounded regions.

SSI problems can be solved by BEM models based on a full-space fundamental solution. However, it requires an additional discretization of the free field around the studied soil area to avoid cut-off errors related with the mesh boundaries. Therefore, the computational effort to solve SSI problems using a full-space solution could dramatically increase. This problem does not appear using a half-space fundamental solution since the free field condition is implicitly satisfied. Soil discretization is limited to those regions differing either from the half-space geometry or the free field condition. In SSI problems, soil discretization only concerns to soil-structure interfaces.

However, a fully general half-space fundamental solution is not available in explicit form. Some solutions were proposed assuming some simplifications. Firstly, Pekeris [22] presented the half-space response for a vertical load and Poisson's ratio $1/4$. Afterwards, Chao [4] extended Pekeris' solution for horizontal forces. Also, Mooney [19] proposed expressions for computing the half-space response excited by a vertical load and arbitrary Poisson's ratio. A general half-space fundamental solution was proposed by Johnson [14]. In that work, the complete solution in implicit form to the Lamb's problem was derived using the Cagniard-de Hoop method by applying Laplace transform with respect to the time and the spatial coordinate. Recently, Kausel [16] has provided a complete set of expressions for the half-space solution.

The number of works that use the time formulation of the BEM and a half-space fundamental solution is quite reduced. Two works were found in the literature review. Firstly, Triantafyllidis [27] presented an approach using Johnson's solution [14]. This work provides a physical meaning of the Green's function terms. Afterwards, Bode et al. [3] proposed a BEM-FEM model to study SSI problems.

The present paper proposes a time domain BEM formulation using the half-space fundamental solution presented by Johnson [14]. The innovative of this work is the effective treatment of the fundamental solution and its implementation in the BEM. The Green's function has two kind of singularities that should be adequately solved to avoid unstable behaviour. A detailed integration procedure is presented. Moreover, internal soil damping is included in the fundamental solution.

The paper is organized as follows. Firstly, the half-space fundamental solution is discussed, singularities are properly treated, and the internal soil damping is added. Afterwards, the BEM formulation based on the previous solution is described emphasising in the time integration of the Green's function. Finally, a comprehensive SSI problem is solved using the proposed methodology.

2 Half-space fundamental solution

In this work, the half-space fundamental solution proposed by Johnson [14] is analysed. Figure 1 shows schematically the problem geometry, where θ is the direct emission angle, r is the distance between the observation point and the source, and ϕ is the azimuth angle between the reference direction x and the projection of r on the plane $z = 0$. The solution for displacements is a second order tensor, $\mathbf{g}(\mathbf{x}, t; \mathbf{x}^i)$, that relates displacements at a point $\mathbf{x}$ due to a Heaviside load applied at $\mathbf{x}^i$. The tensor component g_{lk} represents the k displacement component due to a load applied according to direction l.
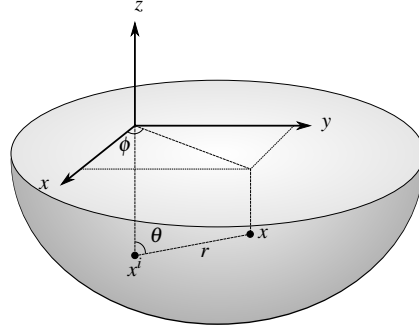

Fig. 1 Problem geometry.

The Green's function for the half-space can be expressed as follows [14]:

$$\mathbf{g}(\mathbf{x}, t; \mathbf{x}^i) = \mathbf{P}(\mathbf{x}, t; \mathbf{x}^i) + \mathbf{S}(\mathbf{x}, t; \mathbf{x}^i) + \mathbf{PP}(\mathbf{x}, t; \mathbf{x}^i)$$
$$+ \mathbf{SS}(\mathbf{x}, t; \mathbf{x}^i) + \mathbf{PS}(\mathbf{x}, t; \mathbf{x}^i) + \mathbf{SP}(\mathbf{x}, t; \mathbf{x}^i) \tag{1}$$

where $\mathbf{P}$ and $\mathbf{S}$ are tensors containing direct P and S wave fields, and $\mathbf{PP}$, $\mathbf{SS}$, $\mathbf{PS}$ and $\mathbf{SP}$ concern to P and S reflected waves in the half-space surface.

The solution of Equation (1) involves the evaluation of expressions as:

$$\mathbf{I} = \text{Re}\left\{ \int_0^{p_w} \frac{\mathbf{R}}{\sigma} \left[\frac{1}{\sqrt{\left(\frac{t}{r}\right)^2 - 1/c_\gamma^2 - p^2}} \right] H\left(t - r/c_\gamma\right) dp \right\} \tag{2}$$

where c_γ is either the P-wave propagation velocity, c_p, or the S-wave propagation velocity, c_s, σ is the Rayleigh function, and the tensor $\mathbf{R}$ accounts for the contribution of different waves. The integration is done from $p = 0$ up to $p = p_w$. The upper integration limit depends on the wave propagation velocities and the distance between the receiver point and the source. The physical meaning of these terms can be found in Reference [14].

Equation (2) presents two kinds of singularities. Firstly, a weak singularity is found at the poles of $\sqrt{(t/r)^2 - 1/c_\gamma^2 - p^2}$. A simple change of variable allows an effective treatment of this singularity [14]:

$$p = \left((t/r)^2 - 1/c_\gamma^2\right)^{1/2} + w^2 \qquad \gamma = p, s \tag{3}$$

where w is the new integration variable.

The second singularity occurs when the direct emission angle is $\theta = \pi/2$, the source and the observation points are located at the half-space surface and, moreover, the time is longer than the arrival time of the Rayleigh waves. This singularity depends on the Rayleigh function poles.

The Rayleigh function is expressed as:

$$\sigma(p) = \left[1/c_s^2 - 2(q^2 - p^2)\right]^2 + 4(q^2 - p^2)\sqrt{1/c_s^2 - (q^2 - p^2)}\sqrt{1/c_p^2 - (q^2 - p^2)} \quad (4)$$

being

$$q(p) = -t\sin(\theta)/r + i\cos(\theta)\sqrt{(t/r)^2 - 1/c_\gamma^2 - p^2} \quad (5)$$

where $i = \sqrt{-1}$.

The homogeneous solution of the Equation (4) yields to the Rayleigh poles, p_R:

$$p_R^2 = \frac{\cot^2(\theta)}{c_\gamma^2} + (-1/c_R^2 + t^2/r^2)\csc^2(\theta) \pm \frac{2t\cos(\theta)\csc^2(\theta)i\sqrt{c_\gamma^2/c_R^2 - 1}}{c_\gamma r} \quad (6)$$

where c_R is the Rayleigh wave propagation velocity.

A strong singularity appears at Rayleigh poles defined by the Cauchy Principal Value. Johnson [14] proposed a refinement of the integration around p_R using the Romberg integration scheme to evaluate the integral. This procedure increases the computational effort and it is unstable for a direct emission angle close to $\pi/2$.

This work proposes an alternative procedure to evaluate integrals as defined by Equation (2) based on the Residue Theorem. The integrals can be solved using a closed complex path to avoid the strong singularity (Figure 2). The integration path is divided into a real path defined between $p = 0$ and $p = p_w$, a deformed branch that excludes the non-analytical points due to P and S wave propagation velocities, $p_p = \sqrt{(t/r)^2 - 1/c_p^2}$ and $p_s = \sqrt{(t/r)^2 - 1/c_s^2}$, and a complex path that closes the integration contour. The Equation (2) is rewritten as follows:
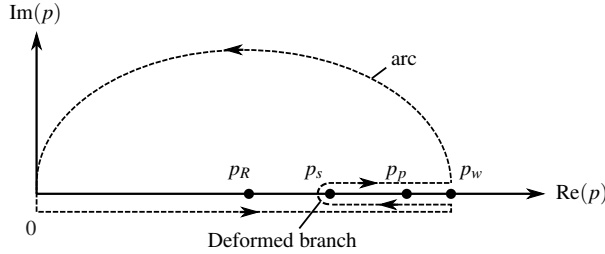

Fig. 2 Complex integration path.

$$\mathbf{I} = \text{Re}\left\{\oint \widehat{\mathbf{R}}\, dp - \int_{def.branch} \widehat{\mathbf{R}}\, dp - \int_{arc} \widehat{\mathbf{R}}\, dp\right\} =$$
$$\text{Re}\left\{2\pi i \, \text{Res}\left(\widehat{\mathbf{R}}, p_R\right) - \int_{def.branch} \widehat{\mathbf{R}}\, dp - \int_{arc} \widehat{\mathbf{R}}\, dp\right\} \quad (7)$$

where $\widehat{\mathbf{R}}$ encloses the integrand in Equation (2), and $\text{Res}\left(\widehat{\mathbf{R}}, p_R\right)$ is the residue of $\widehat{\mathbf{R}}$ at $p = p_R$.

Equation (7) is simplified taking into account that the kernels over the complex path are conjugated:

$$\text{Re}\left\{\int_{def.\ branch} \widehat{\mathbf{R}}\,dp\right\} = \text{Re}\left\{2\int_{p_s}^{p_w} \text{Im}\{\widehat{\mathbf{R}}\}\,dp\right\} = 0 \tag{8}$$

The residue also vanishes when $p = p_R$. This fact is shown by separating $\widehat{\mathbf{R}}$ in two parts, the first one containing the Rayleigh function, σ, and the other one, $\mathbf{N}$, accounts for the rest of parameters. If the integration variable tends to the Rayleigh pole p_R the following identity is obtained:

$$\text{Re}\left\{2\pi i\,\text{Res}\left(\widehat{\mathbf{R}}, p_R\right)\right\} = \text{Re}\left\{2\pi i \lim_{p \to p_R}(p - p_R)\mathbf{N}/\sigma\right\} = \text{Re}\left\{2\pi i\mathbf{N}/\sigma'\right\} \tag{9}$$

where σ' at the Rayleigh pole, p_R, is:

$$\sigma' = \left.\frac{d\sigma(p)}{dp}\right|_{p_R} = 4p_R\left\{-2c_R^4 c_s^2 + 3c_R^2 c_s^4 + c_p^2\left[-4c_s^4 + 2c_R^4\sqrt{(1/c_p^2 - 1/c_R^2)c_s^2}\sqrt{1 - c_s^2/c_R^2} + \right.\right.$$
$$\left.\left. c_R^2 c_s^2\left(3 - 4\sqrt{(1/c_p^2 - 1/c_R^2)c_s^2}\sqrt{1 - c_s^2/c_R^2}\right)\right]\right\} / \left\{c_p^2 c_R^4 c_s^2\sqrt{(1/c_p^2 - 1/c_R^2)c_s^2}\sqrt{1 - c_s^2/c_R^2}\right\} \tag{10}$$

The expression between the brackets in Equation (9) is purely imaginary since $\mathbf{N}$ and σ' are real values. Therefore, the real part of the residue vanishes.

Finally, Equation (2) can be written as follows:

$$\mathbf{I} = \text{Re}\left\{-\int_{arc}\frac{\mathbf{R}}{\sigma}\left[\frac{2}{\sqrt{-w^2 - 2\sqrt{\left(\frac{t}{r}\right)^2 - 1/c_\gamma^2}}}\right]H\left(t - r/c_\gamma\right)dw\right\} \tag{11}$$

Equation (11) does not show any singularity and it is integrated by a simple quadrature rule.

In this paper, the internal soil damping in addition to the radiation soil attenuation is considered. An hysteretic damping model depending on the angular frequency, ω, the distance between the source and the observation point, r, and the S-wave propagation velocity, c_s, is considered:

$$\mathbf{g}_d(\mathbf{x}, \omega; \mathbf{x}^i) = \mathbf{g}(\mathbf{x}, \omega; \mathbf{x}^i)e^{\frac{-i\xi\omega r}{c_s}} \tag{12}$$

where $\mathbf{g}_d(\mathbf{x}, \omega; \mathbf{x}^i)$ denotes the soil response in the frequency domain considering the internal damping. ξ is the hysteretic damping ratio.

Equation (12) is expressed in the time domain by applying the inverse Fourier transform:

$$\mathbf{g}_d(\mathbf{x}, t; \mathbf{x}^i) = \mathbf{g}(\mathbf{x}, t; \mathbf{x}^i) * \frac{c_s r\xi}{\pi(r^2\xi^2 + c_s^2 t^2)} \tag{13}$$

where $*$ means time convolution process.

Equation (13) represents the half-space fundamental solution considering internal soil damping in the time domain. The proposed procedure to evaluate the half-space fundamental solution is low time consuming due to the analytical treatment of the singularities. The traction solution, $\mathbf{f}_d$, is evaluated using the constitutive law for a linear elastic, homogeneous and isotropic solid by computing the spatial derivatives of the Green's function. In the next sections, subscript d will be omitted for a clearer notation.

2.1 Numerical verification

The proposed solution is verified by comparison with known analytical solutions. Pekeris [22] presented an explicit displacement solution for a Heaviside vertical load applied at the half-space surface. Later, Chao [4] extended Pekeris' solution for a horizontal load. Both solution are only valid for a half-space with Poisson's ratio $\nu = 1/4$.

Half-space properties were: P-wave propagation velocity $c_p = 519.6\,\text{m/s}$, S-wave propagation velocity $c_s = 300\,\text{m/s}$, and density $\rho = 1900\,\text{kg/m}^3$. Three different internal damping ratios were considered: $\xi_1 = 0$, $\xi_2 = 0.02$, and $\xi_3 = 0.06$. The response at a point located at $r = 10\,\text{m}$ from the source was analysed.

Numerical results were computed by the non-stabilised integrals defined in Equation (2) and by the methodology proposed in Equation (13). Figure 3 shows the dimensionless displacement, $\widetilde{\mathbf{g}}(\mathbf{x}, \tau; \mathbf{x}^i) = \mathbf{g}(\mathbf{x}, t; \mathbf{x}^i)\mu r\pi/P$, where $\mu = c_s^2/\rho$ is the transversal shear modulus and P is the load amplitude. The response is represented versus dimensionless time $\tau = tc_s/r$. The response shows an initial perturbation at the arrival time of the P-wave ($\tau = 0.57$). The maximum displacement is reached between the arrival time of S-wave ($\tau = 1$) and the arrival time of Rayleigh wave ($\tau = 1.08$). The agreement between the computed results and those obtained from the analytical solution [4,22] is quite good. The internal soil damping induces a smoother behaviour around the different arrival time of the waves. Numerical solution computed by the non-stabilised procedure shows an unstable behaviour after dimensionless time $\tau = 1.08$. These oscillations are eliminated using the proposed integration path.

3 Boundary element formulation

This section presents the three-dimensional (3D) boundary element formulation in time domain based on the half-space fundamental solution previously developed. The integral representation of the displacement u^i for a point i on the soil surface at time t, with zero body forces and zero initial conditions can be written as [8]:

$$c_{lk}^i u_k^i(\mathbf{x}^i, t) = \int_0^{t+} \int_\Gamma u_{lk}^*(\mathbf{x}, t - \tau; \mathbf{x}^i) p_k(\mathbf{x}, \tau) d\Gamma d\tau$$
$$- \int_0^{t+} \int_\Gamma p_{lk}^*(\mathbf{x}, t - \tau; \mathbf{x}^i) u_k(\mathbf{x}, \tau) d\Gamma d\tau \tag{14}$$

where u_k and p_k stand for the k component of the displacement and traction, respectively; $u_{lk}^*(\mathbf{x}, t - \tau; \mathbf{x}^i)$ and $p_{lk}^*(\mathbf{x}, t - \tau; \mathbf{x}^i)$ are the half-space fundamental solution displacement and traction tensors, respectively, at point $\mathbf{x}$ due to an impulsive load applied at $\mathbf{x}^i$ in l direction. The integral-free term c_{lk}^i depends only on the boundary geometry at point $\mathbf{x}^i$, and its value is unitary at the soil surface for a smooth boundary. For non-smooth boundaries c_{lk}^i is computed as presented in Reference [17].

Half-space fundamental solution for an impulsive load is derived from the solution for a Heaviside load as:

$$u_{lk}^*(\mathbf{x}, t; \mathbf{x}^i) = \frac{\partial g_{lk}(\mathbf{x}, t; \mathbf{x}^i)}{\partial t} \tag{15}$$

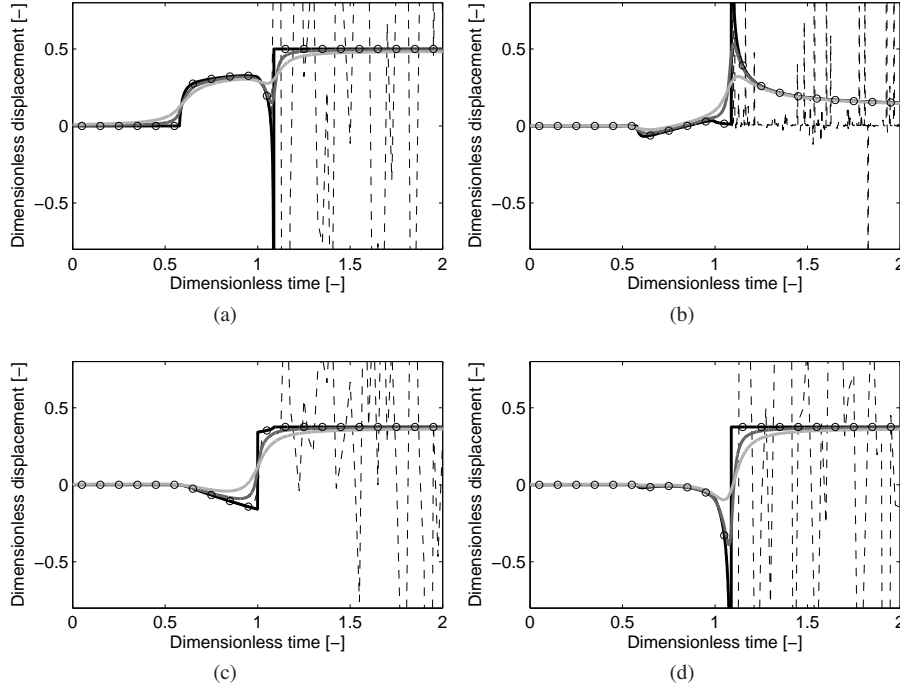$$p_{lk}^*(\mathbf{x}, t; \mathbf{x}^i) = \frac{\partial f_{lk}(\mathbf{x}, t; \mathbf{x}^i)}{\partial t} \tag{16}$$

Fig. 3 Soil surface dimensionless displacement, $\widetilde{\mathbf{g}}(\mathbf{x}, \tau; \mathbf{x}^i)$, for a point located at $r = 10\,\text{m}$ from the source due to a Heaviside load: (a) $\widetilde{g}_{11}$, (b) $\widetilde{g}_{31}$, (c) $\widetilde{g}_{22}$, and (d) $\widetilde{g}_{33}$. Analytical solution [4, 22] (circles), non-stabilized solution (dashed black line), and proposed method for internal damping $\xi_1 = 0$ (black solid line), $\xi_2 = 0.02$ (dark grey solid line), and $\xi_3 = 0.06$ (light grey solid line).

Displacements and tractions over the boundary are approximated at the time step $t = n\Delta t$ from their nodal values u_k^{mj} and p_k^{mj}, using the space interpolation functions $\phi^j(r)$ and $\psi^j(r)$, and the time interpolation functions $\eta^m(\tau)$ and $\mu^m(\tau)$ as:

$$
c_{lk}^i u_k^i(\mathbf{x}^i, t) = \sum_{m=1}^{n} \sum_{j=1}^{Q} \left\{ \left[\int_{\Gamma_j} \int_{\Delta t_m} u_{lk}^*(\mathbf{x}, t - \tau; \mathbf{x}^i) \mu^m d\tau \psi^j d\Gamma \right] p_k^{mj} \right.
$$
$$
\left. - \left[\int_{\Gamma_j} \int_{\Delta t_m} p_{lk}^*(\mathbf{x}, t - \tau; \mathbf{x}^i) \eta^m d\tau \phi^j d\Gamma \right] u_k^{mj} \right\}
\tag{17}
$$

where Q is the total number of boundary nodes and Γ_j represents the elements to which node j belongs.

Time kernels in Equation (17) are analytically integrated using constant and linear piecewise time interpolation functions $\mu^m(\tau)$ and $\eta^m(\tau)$ for tractions and displacements, respec-

tively:

$$
\begin{aligned}
U_{lk}^{nm} &= \int_{\Delta t_m} u_{lk}^*(\mathbf{x}, t-\tau; \mathbf{x}^i)\mu^m d\tau \\
&= g_{lk}(\mathbf{x}, [n-m+1]\Delta t; \mathbf{x}^i) - g_{lk}(\mathbf{x}, [n-m]\Delta t; \mathbf{x}^i)
\end{aligned}
\tag{18}
$$

$$
\begin{aligned}
P_{lk}^{nm} &= \int_{\Delta t_m} p_{lk}^*(\mathbf{x}, t-\tau; \mathbf{x}^i)\eta^m d\tau = 1/\Delta t \left\{ F_{lk}(\mathbf{x}, [n-m+1]\Delta t; \mathbf{x}^i) \right. \\
&\left. -2F_{lk}(\mathbf{x}, [n-m]\Delta t; \mathbf{x}^i) + F_{lk}(\mathbf{x}, [n-m-1]\Delta t; \mathbf{x}^i) \right\}
\end{aligned}
\tag{19}
$$

where $\mathbf{F}(\mathbf{x}, t; \mathbf{x}^i)$ is the time integral of the traction tensor $\mathbf{f}(\mathbf{x}, t; \mathbf{x}^i)$. This integral is easily computed considering that the tensor $\mathbf{f}(\mathbf{x}, t; \mathbf{x}^i)$ presents implicitly a time derivative [14].

After interpolating the boundary variables, the integral equation (17) becomes:

$$
c_{lk}^i u_k^i(\mathbf{x}^i, t) = \sum_{m=1}^n \sum_{j=1}^Q \left\{ \left[\int_{\Gamma_j} U_{lk}^{nm} \psi^j d\Gamma \right] p_k^{mj} - \left[\int_{\Gamma_j} P_{lk}^{nm} d\tau \phi^j d\Gamma \right] u_k^{mj} \right\}
\tag{20}
$$

Equation (20) is written in a more compact form as:

$$
c_{lk}^i u_k^{ni} = \sum_{m=1}^n \sum_{j=1}^Q \left[G_{lk}^{nmij} p_k^{mj} - \widehat{H}_{lk}^{nmij} u_k^{mj} \right]
\tag{21}
$$

Once the integral-free term c_{lk}^i is included in the system matrix, the integral representation for point i at time $t = n\Delta t$ becomes:

$$
\mathbf{H}^{nn}\mathbf{u}^n = \mathbf{G}^{nn}\mathbf{p}^n + \sum_{m=1}^{n-1} \left[\mathbf{G}^{nm}\mathbf{p}^m - \mathbf{H}^{nm}\mathbf{u}^m \right]
\tag{22}
$$

where H_{lk}^{nmij} collects for c_{lk}^i when $i = j$ and $n = m$.

In this work nine-node rectangular quadratic boundary elements are used. Identical space interpolation shape functions $\phi^j(r)$ and $\psi^j(r)$ are assumed. The spatial integration is done only in those parts of an element under the effects of the fundamental solution waves, according to the causality condition of each term of the fundamental solution [18]. Each side of the element is divided into equal parts in the natural coordinate domain yielding an element subdivision.

Equation (22) yields a system of equations that is solved step by step to obtain the time variation of displacements and tractions at the boundary. After boundary unknowns are solved, the radiated wave field $\mathbf{u}_r^n$ at any internal point or at the free field is computed by means of the integral representation of the Somigliana identity:

$$
\mathbf{u}_r^n = \sum_{m=1}^n \left(\mathbf{G}_r^{nm}\mathbf{p}^m - \widehat{\mathbf{H}}_r^{nm}\mathbf{u}^m \right)
\tag{23}
$$

where $\mathbf{G}_r^{nm}$ and $\widehat{\mathbf{H}}_r^{nm}$ are the boundary element matrices computed considering only domain point as source points.

The BEM performance is enhanced taking into account dimensionless expressions for the fundamental solution, $\widetilde{\mathbf{g}}(\mathbf{x}, \tau, \mathbf{x}^i) = \mathbf{g}(\mathbf{x}, t, \mathbf{x}^i)\mu r\pi/P$, and the time vector, $\tau = tc_s/r$. Then, the fundamental solution is computed considering cylindrical coordinate system as:

$$
\widetilde{\mathbf{g}}^{cyl}(\mathbf{x}, \tau; \mathbf{x}^i) = \frac{\mu r\pi}{P} \begin{bmatrix} \widetilde{g}_{rr} & 0 & \widetilde{g}_{rz} \\ 0 & \widetilde{g}_{\phi\phi} & 0 \\ \widetilde{g}_{zr} & 0 & \widetilde{g}_{zz} \end{bmatrix}
\tag{24}
$$

The fundamental solution in the cartesian coordinate system is obtained transforming the Equation (24) for each integration element:

$$\widetilde{\mathbf{g}} = \mathbf{\Omega} \widetilde{\mathbf{g}}^{cyl} \mathbf{\Omega}^T \tag{25}$$

where $\mathbf{\Omega}$ is the transformation matrix from cylindrical to cartesian coordinate system:

$$\mathbf{\Omega} = \begin{bmatrix} \cos\phi & \sin\phi & 0 \\ -\sin\phi & \cos\phi & 0 \\ 0 & 0 & 1 \end{bmatrix} \tag{26}$$

Equation (24) represents an antisymmetrical second order tensor. This dimensionless fundamental solution does not depend on the distance from the source to the observation point when the direct emission angle is $\theta = \pi/2$. In this case, Equation (24) is computed just once and it is transformed for each collocation point and integration element.

Several test have shown that the evaluation of the fundamental solution should be extended, at least, three times after the arrival time of the Rayleigh wave, i.e., $\tau = 4.32$.

3.1 Numerical validation

The soil response due to a vertical Heaviside point load is studied to validate the proposed BEM formulation. The computed results are compared with analytical solution presented by Pekeris [22], and with numerical results presented by Triantafyllidis [27] and Bode et al. [3]. This benchmark problem has been previously used by Rizos and Karabalis [24] and by Romero et al. [25] to validate different boundary element formulations based on full space fundamental solutions.

A half-space with the following properties was studied: $c_p = 519.6$ m/s, $c_s = 300$ m/s, and $\rho = 1900$ kg/m^3. Three different internal soil damping ratios were considered: $\xi_1 = 0$, $\xi_2 = 0.02$, and $\xi_3 = 0.06$. The soil surface was discretized by one boundary element with a characteristic length $\Delta l = 0.5\sqrt{2}/2$ m (Figure 4). A load, $p(t) = 1H(t)$ N, was applied at the central node of the element. Soil response was computed at a semicircular grid of 5151 receivers located in the free field and inside the soil.
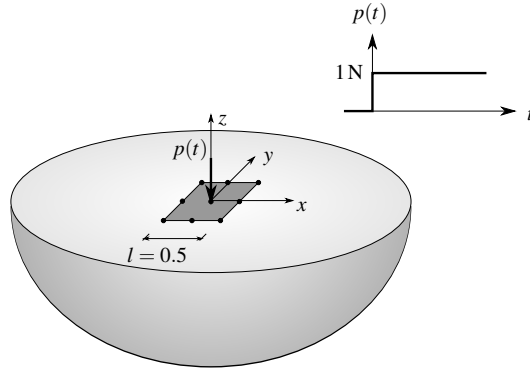

Fig. 4 Half-space representation excited by a Heaviside load.

The time step was set at $\Delta t = 4 \times 10^{-4}$ s in order to avoid stability problems [18]. The selected time step and element size give a value of the stability parameter $\beta = c_s \Delta t / \Delta l = 0.34$.

Figure 5 shows the time history of the soil response for a point located at 10 m from the source. Results are plotted in dimensionless form as it was done in the previous section. Numerical results were compared with analytical solution [22] in good agreement. The maximum discrepancies occurred at the arrival time of Rayleigh waves. The accuracy was related with the distance between the observation point and the source element, due to the influence of the load representation from the element shape functions. Moreover, the time between the arrival of the P-wave and the Rayleigh wave depends on the distance to the observation point, being $\Delta t_{c_p - c_R} = 0.51 r / c_s$ (Section 2.1). Therefore, a thinner time discretization is required for computing the transient response at points close to the source, and a reduction of the element size is needed to ensure an accurate and stable solution.
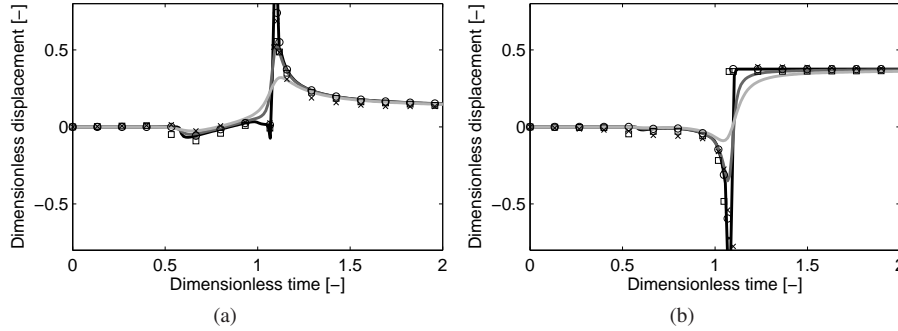

Fig. 5 Time history of (a) horizontal and (b) vertical displacements due to a vertical Heaviside point load: analytical solution [22] (circles), numerical results presented by Triantafyllidis [27] (crosses) and Bode et. al [3] (squares), and computed results from the proposed methodology for $\xi_1 = 0.00$ (black line), $\xi_2 = 0.02$ (dark grey line) and $\xi_3 = 0.06$ (light grey line).

The computed results were also compared with numerical solutions presented by Triantafyllidis [27] and Bode et al. [3]. In the first case, results were computed for a direct emission angle $\theta = \pi/2 - \varepsilon$ being $\varepsilon = 0.0198$ rad, to avoid unstable results. The agreement between the different results is quite good. However, the proposed methodology allows to consider both source and observation points at the half-space surface ($\theta = \pi/2$) without any instabilities, and to represent the internal soil damping.

Figure 6 shows dimensionless soil displacements at time $t = 0.0092$ s. Soil response presents two wave fronts due to P-wave and S-wave at radial distances $r_p = 4.8$ m and $r_s = 2.8$ m from the source, respectively. The Rayleigh wave front can be found at a radius $r_R = 2.5$ m. The Rayleigh wave dominates the soil surface response and its influence becomes lower as the soil depth increases, while P-wave and S-wave are prevailing into the soil.

4 Coupled BEM-FEM formulation

This work uses the `SSIFiBo` toolbox for `MATLAB` previously developed by Galvín and Romero [11, 12]. The SSI problem is decomposed in two subdomains represented by the BEM and the FEM. Coupling of both methods requires that the equilibrium of forces and the compatibility of displacements are fulfilled at the interface between the two subdomains. The coupling is performed directly and the equations of both subdomains are assembled into
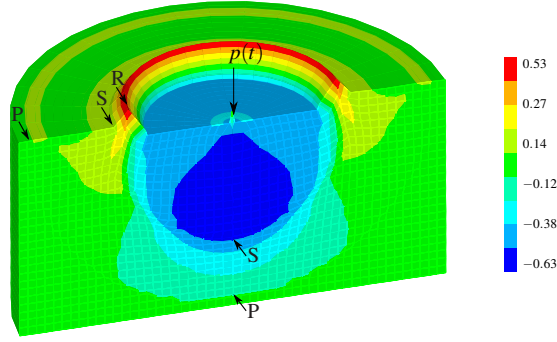
Fig. 6 Dimensionless soil response at time $t = 0.0092$ s due to a vertical Heaviside point load applied at soil surface.

a global system of equations. The FEM equation is solved at each time step following an implicit time integration GN22 Newmark method [20, 29].

5 Numerical example

In this section, the dynamic behaviour of a framed wall building subjected to three different loads (an uniform incident wave field, the ground-borne vibrations induced by a moving load, and a seismic load) is studied.

The analysis of the wave propagation problem is done by decomposition of the total wave field in two terms: the incident and the scattered fields [8]. The wave propagation is solved by Equation (22). Once the scattered wave field is obtained, the incident wave field is superimposed to the radiation problem (Equation (23)).

The dimensions of the studied twelve-storey building were 12 m $\times 12$ m $\times 36$ m (Figure 7). The structure consisted of eight concrete columns with 0.6 m $\times 0.4$ m section, four edge beams with 0.6 m $\times 0.2$ m section, and two framed concrete wall with 2.4 m $\times 0.15$ m section. The floors were simply supported concrete slabs with a thickness of 0.2 m. The floors consist of a two-dimensional frame with axial stiffness per unit length $EA = 1.433 \times 10^9$ N/m, bending stiffness per unit length $EI = 9.935 \times 10^6$ Nm, and a mass per unit area of $m = 172$ kg/m^2. The structure was founded on a 1.0 m thick concrete slab. The concrete material had the following properties: Young's modulus $E = 20 \times 10^9$ N/m^2, Poisson's ratio $\nu = 0.2$ and density $\rho = 2400$ kg/m^3.

The structural damping was considered by a Rayleigh model [5]. The damping matrix, $\mathbf{C} = a_0\mathbf{M} + a_1\mathbf{K}$, was computed proportional to the mass, $\mathbf{M}$, and the stiffness, $\mathbf{K}$, matrices. A structural damping, $\zeta = 5\%$, was set for the first and second mode shapes. Proportional constant values were $a_0 = 0.4193$ s^{-1} and $a_1 = 0.0042$ s.

The structure was discretized by 1248 two-node Euler-Bernoulli beam elements to represent columns and beams, and 3072 four-node shell elements for considering the floors and the framed walls. Figure 7.(b) shows the discretization of the building. The element size varies from 0.5 m to 1.25 m. This length was enough to represent adequately the structure dynamic behaviour.

The soil was represented as an elastic half-space. Soil discretization extends only to soil-structure interface using 48 nine-node rectangular quadratic boundary elements. Three different soils were studied. The time step was chosen according to each soil properties to
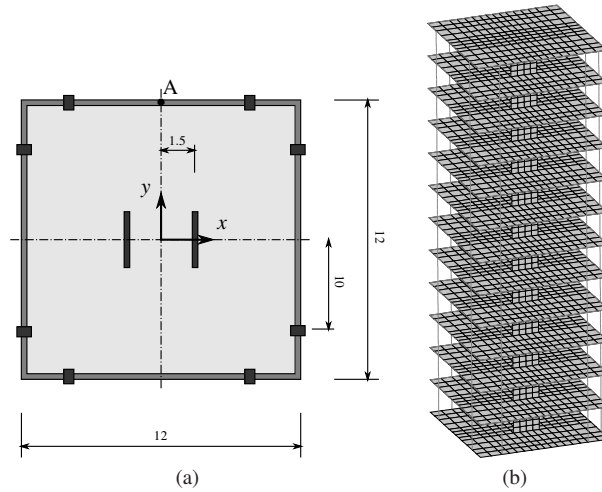
Fig. 7 (a) Building plan geometry and (b) discretization.

ensure the stability of the methodology, setting the β parameter between 0.42 and 0.7. Soil properties and time steps are presented in Table 1.

Soil type	c_p [m/s]	c_s [m/s]	ρ [kg/m^3]	Δ t [s]
Stiff	995.0	300	1600	2.25×10^{-3}
Medium	497.5	150	1600	4.50×10^{-3}
Soft	165.8	50	1600	1.35×10^{-2}

Table 1 Soil properties and time steps for the analysis.

5.1 Building behaviour due to incident wave field

In this example, the building response due to an uniform incident wave field is analysed. Oliveto and Santini [21] studied the same building with a simplified model. These authors modelled the building as a plane frame, and a wall linked to each floor by inextensible bar elements. The masses were lumped at the floors levels. The structure was founded on a rigid circular plate and a transfer matrix was used to represent the soil.

The incident wave fields corresponded with plane SH and SV waves propagating along x-axis. The incident waves induced an uniform acceleration at the soil-structure interface, $a(\mathbf{x},t) = 1\delta(t)$ m/s^2, where δ is the Dirac delta function.

Firstly, the horizontal building response computed with the proposed method for a SH incident wave is compared with the results presented by Oliveto and Santini [21]. Bending floor stiffness was neglected for comparison purposes. Stiff and soft soils were analysed. Figure 8 shows the time history of the horizontal displacement in the y-direction at the ground, and the fourth, sixth and twelfth floors. Results for the observation point A (Figure 7.(a)) are shown. The floor responses were in phase and their amplitudes increased with

the level floor. The amplitudes decreased according to the structural damping and the soil effects. The characteristic period of the response was higher for soft soil due its higher flexibility.
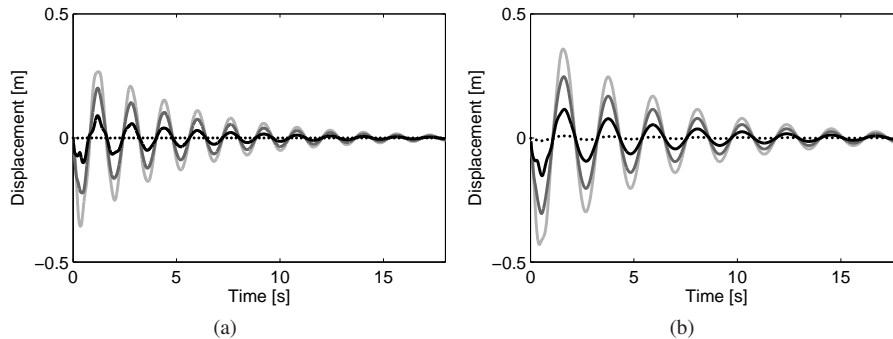

(a)

(b)

Fig. 8 Time history of the horizontal displacement along y-direction at the observation points A located at ground floor (black dotted line), and 4th (black solid line), 6th (dark grey solid line), and 12th (light grey solid line) floors for a building founded on (a) stiff soil and (b) soft soil.

Figure 9 presents the frequency content of the building response considering the stiffer soil. The structure response considering fixed base is also shown. Both results were compared with the numerical solution presented by Oliveto and Santini [21]. Frequency response has been obtained by applying a direct Fourier Transform to the time history. The computed response shows two peaks at the resonance frequencies given by $f_1 = 0.64$ Hz and $f_2 = 2.35$ Hz. These frequencies correspond with transversal mode shapes along y-direction. The agreement with the reference solution presented by Oliveto and Santini is quite good. The computed resonance frequencies were slightly higher, which it indicates a stiffer model.
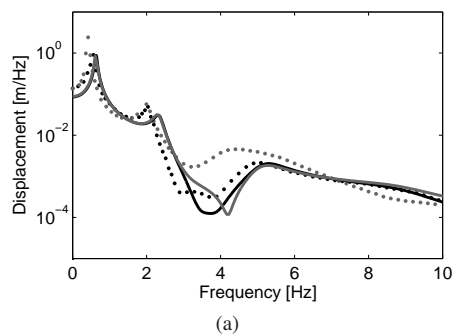

(a)

Fig. 9 Frequency content of the horizontal displacement along y-direction at observation point A located at the top floor for a building founded on the stiff soil: fixed based (black line) and proposed BEM-FEM method (grey line), and Oliveto and Santini's results [21] considering fixed based (black points) and considering soil-structure interaction (grey points).

The effect of the soil flexibility caused a change in the resonance frequencies that moved to lower values as the soil became softer (Figure 10.(a)). Figure 10.(b) shows the amplitudes at the first resonance frequency plotted versus floor level for each type of soil. Maximum amplitude was observed for the softest soil.
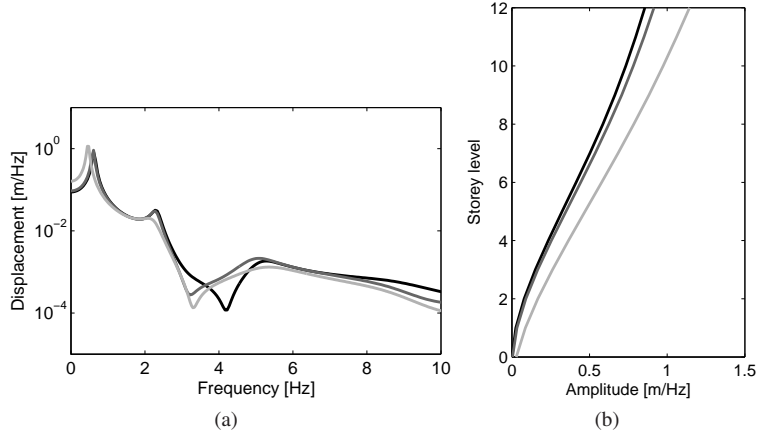

(a)   (b)

Fig. 10 (a) Frequency content of the horizontal displacement along *y*-direction at the observation point *A* located at the top floor and (b) amplitude at the first resonance frequency at each floor, for a building founded on stiff soil (black line), medium soil (dark grey line), and soft soil (light grey line).

Once the proposed method was tested with the reference solution [21], the building response was analysed considering both axial and bending floor stiffness. Structural behaviour was found similar. However, bending floor stiffness produced a structure stiffening at the floors and the framed wall connection [13]. The resonance frequencies were higher and the amplitudes decreased in relation with the model only account for axial floor stiffness (Figure 11). Table 2 summarizes these results. Building deflection shapes at the first and the second translational resonance frequencies considering the medium soil are shown in Figure 12. Deflection shapes were normalized to the maximum amplitude.

Floor model	Soil type	1st resonance frequency		2nd resonance frequency	
		Frequency [Hz]	Amplitude [m]	Frequency [Hz]	Amplitude [m]
Axial stiffness	Fixed based	0.64	0.872	2.32	0.031
	Stiff	0.63	0.856	2.30	0.032
	Medium	0.61	0.915	2.28	0.031
	Soft	0.46	1.445	2.08	0.020
Axial and bending stiffness	Fixed based	0.86	0.466	2.91	0.018
	Stiff	0.84	0.448	2.89	0.019
	Medium	0.79	0.523	2.87	0.018
	Soft	0.53	0.817	2.74	0.009

Table 2 Resonance frequencies and amplitudes for the first and the second mode shapes considering only axial floor stiffness, and axial and bending floor stiffness.
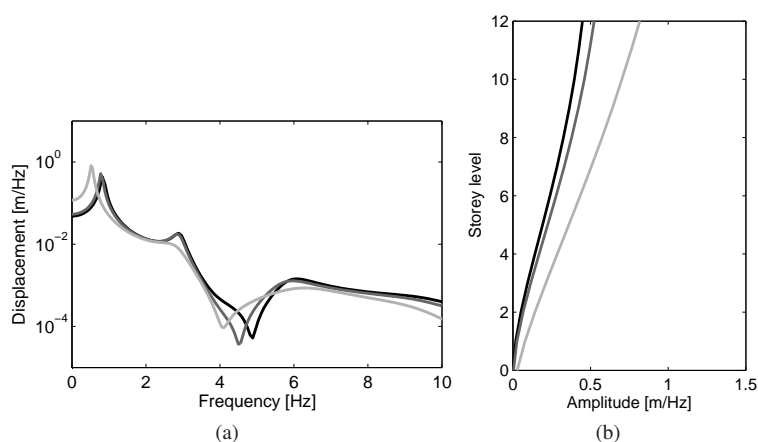
(a)   (b)

Fig. 11 (a) Frequency content of the horizontal displacement along y-direction at the observation point A located at the top floor and (b) amplitude at the first resonance frequency at each floor, for a building founded on stiff soil (black line), medium soil (dark grey line), and soft soil (light grey line). Axial and bending floor stiffness are considered.
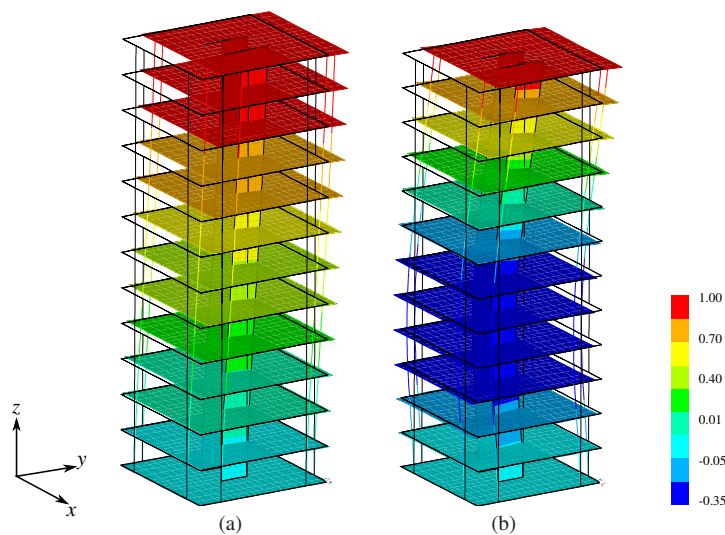

(a)   (b)

Fig. 12 Building response due to an incident wave field applied in y-direction: (a) $f_1 = 0.86\,\text{Hz}$ and (b) $f_2 = 2.91\,\text{Hz}$.

The SSI influence on the vertical response due to a SV wave field is more important than on the horizontal one. Figure 13.(a) shows the frequency content of the vertical displacement at the twelfth floor for each analysed soil. The floor response showed a peak at $f_3 = 8.8\,\text{Hz}$ for the stiffest soil. However, the structural behaviour changed for softer soils. Two peaks appeared at frequencies $f_3 = 4.0\,\text{Hz}$ and $f_4 = 10.0\,\text{Hz}$ for a medium soil. These

peaks moved to lower frequencies when the softest soil was considered. In this case, the resonance frequencies were $f_3 = 0.6\,$Hz and $f_4 = 7.0\,$Hz.

Figure 13.(b) shows the amplitude at the third resonance frequency at each floor for the different studied soil. The building response at the ground and at the first floor presented a significant difference because of the stiffness of the foundation. The soil flexibility caused a global translational displacement on the structure. The floor responses increased with the level.

Figure 14 shows the building response at two resonance frequencies for the medium soil. The deflection shape presented a large translational displacement at the foundation, specially at the resonance frequency $f_3 = 4.0\,$Hz.

(a)   (b)
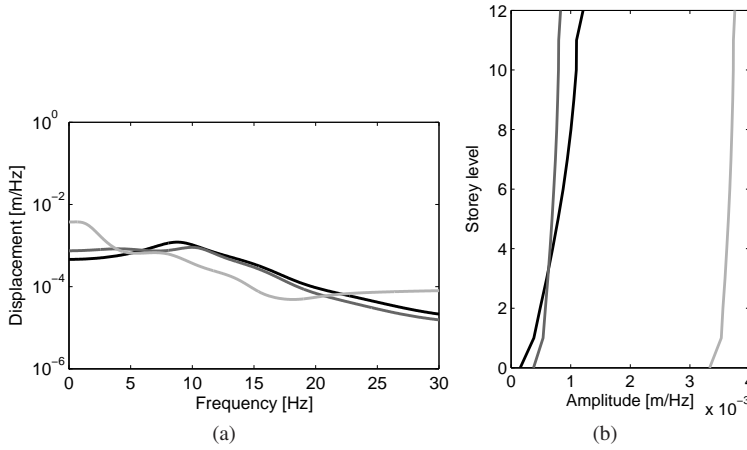
Fig. 13 (a) Frequency content of the vertical displacement at the observation point A located at the top floor and (b) amplitude at the resonance frequency f_3, for a building founded on stiff soil (black line), medium soil (dark grey line), and soft soil (light grey line). Axial and bending floor stiffness are considered.

The previous results show that the proposed methodology allows to describe the dynamic SSI due to incident wave fields. In this case, the building response due to a transversal wave field was determined by the translational mode shapes. The structural behaviour due to vertical waves is highly influenced by the soil flexibility.

5.2 Dynamic response due to a moving load

This example concerns with the building response due to a vertical load travelling at constant speed. the ground-borne vibrations were computed from the analytical solution proposed by Barber [2]. The structure was subjected to this incident wave field. This procedure is only valid if the structure is far enough from the load and its influence is negligible.

The load moved according to a straight line located at $y = 26\,$m from the building (Figure 15) at speed $v = 97.2\,$m/s. Load travelled from $x_i = -696\,$m to $x_f = 1274\,$m, and its value was $P = 170 \times 10^3$ N. The medium soil with internal damping $\xi = 0.06$ (Table 1) was considered.

Figure 16 shows soil and building responses at three time steps: $t_1 = 6.88\,$s, $t_2 = 6.98\,$s, and $t_3 = 7.08\,$s. These times correspond with load passage at $x_1 = -16\,$m, $x_2 = 0\,$m, and
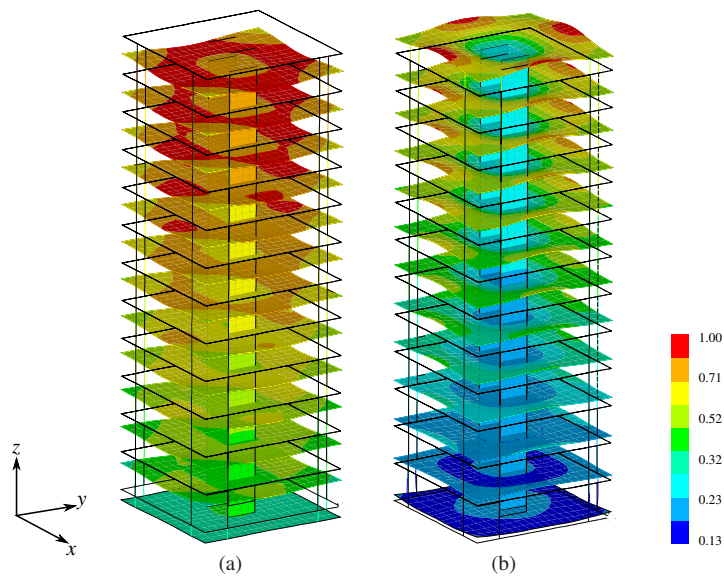
Fig. 14 Building response due to an incident wave field applied in z direction: (a) $f_3 = 4.0$ Hz and (b) $f_4 = 10.0$ Hz.

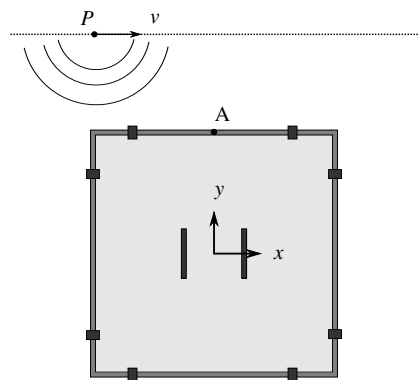**Fig. 15** Geometry of the building excited by a moving load.

$x_3 = 16$ m. Soil and building displacements are represented in different scale for showing soil and building deformed shapes. The load travelled in sub-Rayleigh regime ($v < c_R$). Therefore, the induced wave field was symmetric around the load. The structure response was delayed with the load passage. The maximum displacement occurred at the top floor and at the third time step considered.

Figure 17.(a) shows the time history for the vertical displacements at the observation point A at the ground, and at the sixth, and at the twelfth floors. Maximum vertical displacement occurred at time $t = 7.1$ s when the load was in front of the observation point. The structural response was damped after the load pass, and exhibited oscillations according to
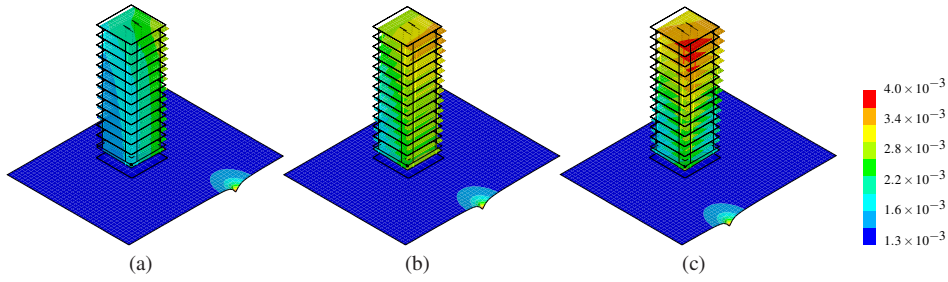
Fig. 16 Soil and building displacements due to a moving load travelling at $v = 97.2\,$m/s at time steps: (a) $t_1 = 6.88\,$s, (b) $t_2 = 6.98\,$s and (c) $t_3 = 7.08\,$s. Colorbar is valid for building response.

its first characteristic period, $T_1 = 1.19\,$s. Maximum displacements amplitude was reached at the top floor.

Figure 17.(b) compares the mobility at different floor levels. The structural behaviour due to the load passage was dominated by the first mode shape at frequency $f_1 = 0.86\,$Hz, and it also appeared a peak at $f_R = 21.0\,$Hz. The characteristic wavelength of the Rayleigh propagation velocity ($c_R = 141\,$m/s) at frequency f_R matches almost exactly with the half of the length of the foundation ($\lambda_R = v/f_R = 6.71\,$m). Moreover, a low level peak was detected at 12.75 Hz related with the Rayleigh wavelength. These wavelengths induced a periodic excitation in the building. The wavelengths did not match exactly with the building size due to the Doppler effect: the response at fixed receivers due to a harmonic moving load travelling at speed v is determined in a frequency range defined by a characteristic phase velocity, c, as $[\omega(1 - v/c), \omega(1 + v/c)]$ [7].
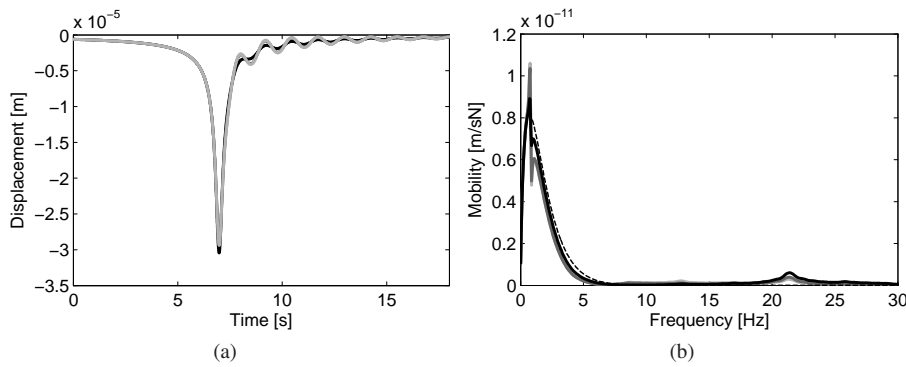

Fig. 17 (a) Time history and (b) mobility of the vertical displacement due to a moving load travelling at $v = 92.7\,$m/s at observation point A located at ground (solid black line), and 6th (solid dark grey line), and 12th (solid light grey line) floors. The mobility of the incident wave field (dashed black line) is also represented.

5.3 Dynamic response due to El Centro (1940) earthquake

Finally, the dynamic behaviour of the building due to El Centro (1940) seismic accelerogram is evaluated. The y-direction was considered coincident with the North-South (NS) earthquake component. Earthquake accelerogram was described as an incident wave field. The accelerations were twice integrated to compute the incident displacement. The computed signal was filtered with a third order Chebyshev highpass digital filter, with a cut off frequency $f_c = 1\,\mathrm{Hz}$. The medium soil with internal damping ratio, $\xi = 0.06$, was also studied in this example.

The earthquake accelerogram induced the maximum amplification at the top floor as can be seen in Figures 18.(a,b). The time histories of the floor responses showed a maximum peak acceleration around $6\,\mathrm{m/s^2}$ in the transversal direction, while low level acceleration was found at the vertical direction.

Figures 18.(c,d) show the response spectra of the acceleration for El Centro earthquake and the building. The response spectra was computed for a period response from $T_i = 0.01\,\mathrm{s}$ to $T_f = 10\,\mathrm{s}$, with a time step $\Delta T = 5 \times 10^{-3}\,\mathrm{s}$, and damping oscillator $\zeta = 0.05$ [5]. El Centro accelerogram was characterized by energy distribution over a frequency range below $20\,\mathrm{Hz}$. The structural response amplification was large at low frequencies, and it became much lower at higher frequencies. Amplifications of the horizontal response occurred at frequencies around $f_1 = 0.86\,\mathrm{Hz}$ and $f_2 = 3.03\,\mathrm{Hz}$ corresponding with the first and second mode shapes, respectively. A resonance was also found at the vertical building response at the fourth mode shape, $f_4 = 10\,\mathrm{Hz}$. Both acceleration components were highly amplified with the floor level.

6 Conclusions

This paper has developed a time domain BEM formulation using Green's function for the half-space as the fundamental solution. This methodology was used together with the FEM to study soil-structure interaction problems.

The half-space fundamental solution is advantageous because of soil discretization is limited to soil-structure interface. However, the solution has two kind of singularities related to the arrival time of the Rayleigh waves. An effective treatment of this singularities that allows a low time consuming evaluation of the solution has been proposed. Visco-elastic soil behaviour is accounted for using an approximation based on an hysteretic damping model. The proposed fundamental solution has been verified with a benchmark problem.

A BEM formulation using the previously analysed half-space solution has been presented. The fundamental solution can be written in dimensionless form to reduce the computational effort of the BEM. It is only evaluated once during the analysis.

The proposed methodology was used to study the dynamic response of a building subjected to different sources: a horizontal and vertical uniform wave fields, a moving load, and an earthquake defined by El Centro (1940) accelerogram. Next conclusions were obtained:

– Horizontal incident wave field excited low frequencies mode shapes related to the deformation of the global structure. Vertical incident wave field induced local deformation at the floors at higher frequencies. In both cases, maximum amplitudes were found at the top floor.
– SSI modified the structural behaviour. The resonance frequencies moved to lower values, and the vertical mode shapes changed for softer soils due to the influence of the soil-foundation system.
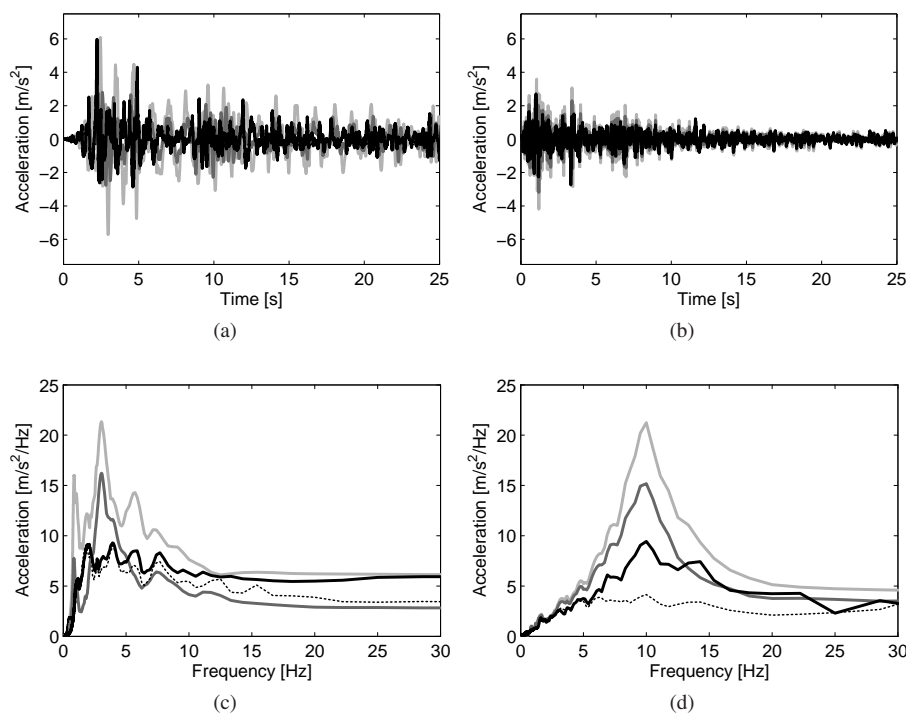
Fig. 18 (a,b) Time history and (c,d) response spectra of the (a,c) *y* component and (b,d) vertical component at the observation point *A* located at ground (black line), and 6th (dark grey line), and 12th (light grey line) floors due to El Centro (1940) earthquake (dotted black line).

– Building response induced by a moving load was determined by its resonance frequencies. In addition, Rayleigh phase wavelengths contributed to the building response when they matched with the structure foundation characteristic length.

References

1. Araújo, F.C., Mansur, W.J., Nishikava, L.K.: Linear θ time-marching algorithm in 3D BEM formulation for elastodynamics. Engineering Analysis with Boundary Elements **23**(10), 825–833 (1999)
2. Barber, J.R.: Surface displacements due to a steadily moving point force. Journal of Applied Mechanics, Transactions ASME **63**(2), 245–250 (1996)
3. Bode, C., Hirschauer, R., Savidis, S.A.: Soil-structure interaction in the time domain using halfspace Green's functions. Soil Dynamics and Earthquake Engineering **22**(4), 283–295 (2002)

4. Chao, C.C.: Dynamical response of an elastic half-space to tangential surface loadings. Journal of Applied Mechanics, Transactions of the ASME **27**(3), 559–567 (1960)
5. Clough, R.W., Penzien, J.: Dynamic of Structures. McGraw-Hill, New York (1975)
6. Clouteau, D., Cottereau, R., Lombaert, G.: Dynamics of structures coupled with elastic media - A review of numerical models and methods. Journal of Sound and Vibration **332**(10), 2415–2436 (2013)
7. Ditzel, A., Herman, G.C., Drijkoningen, G.G.: Seismograms of moving trains: a comparison of theory and measurements. Journal of Sound and Vibration **248**(4), 635–652 (2001)
8. Domínguez, J.: Boundary elements in dynamics. Computational Mechanics Publications and Elsevier Aplied Science, Southampton (1993)
9. Eringen, A.C., Suhubi, E.S.: Elastodynamics, Volume 2, Linear theory. Academic Press, New York, USA (1975)
10. Galvín, P., Domínguez, J.: Analysis of ground motion due to moving surface loads induced by high-speed trains. Engineering Analysis with Boundary Elements **31**(11), 931–941 (2007)
11. Galvín, P., Romero, A., Domínguez, J.: Fully three-dimensional analysis of high-speed train-track-soil-structure dynamic interaction. Journal of Sound and Vibration **329**(24), 5147–5163 (2010)
12. Galvín, P., Romero, A.: A MATLAB toolbox for soil-structure interaction analysis with finite and boundary elements. Soil Dynamics and Earthquake Engineering **57**, 10–14 (2014)
13. Heidebrcht, C., Stafford-Smith, B.: Approximate analysis of tall wall-frame structures. Structural Division **99**, 199–221 (1973)
14. Johnson, L.R.: Green's Function for Lamb's Problem. Geophysical Journal of the Royal Astronomical Society **37**(1), 99–131 (1974)
15. Kausel, E.: Early history of soil-structure interaction. Soil Dynamics and Earthquake Engineering **30**(9), 822–832 (2010)
16. Kausel, E.: Lamb's problem at its simplest. Proceedings of the Royal Society A: Mathematical, Physical and Engineering Sciences **469**(2149) (2013)
17. Mantic, V.: A new formula for the C-matrix in the Somigliana identity. Journal of Elasticity **33**(3), 191–201 (1993)
18. Marrero, M., Domínguez, J.: Numerical behavior of time domain BEM for three-dimensional transient elastodynamic problems. Engineering Analysis with Boundary Elements **27**(1), 39–48 (2003)
19. Mooney, H.M.: Some numerical solutions for Lamb's problem. Bulletin of the Seismological Society of America **64**(2), 473–491 (1974)
20. Newmark, N.M.: A method of computation for structural dynamics. ASCE Journal of the Engineering Mechanics Division **85**(1), 67–94 (1959)
21. Oliveto, G., Santini, A.: A simplified model for the dynamic soil-structure interaction of planar frame-wall systems. Engineering Structures **15**, 431–437 (1992)
22. Pekeris, C.L.: The seismic surface pulse. Proceedings of the National Academy of Sciences of the United States of America **41**, 469–480 (1955)
23. Rizos, D.C., Karabalis, D.L.: An advanced direct time domain BEM formulation for general 3-D elasto-dynamic problems. Computational Mechanics **15**(3), 249–269 (1994)
24. Rizos, D.C., Karabalis, D.L.: A time domain BEM for 3-D elastodynamic analysis using the B-spline fundamental solutions. Computational Mechanics **22**(1), 108–115 (1998)
25. Romero, A., Galvín, P., Domínguez, J.: 3D non-linear time domain FEM–BEM approach to soil–structure interaction problems. Engineering Analysis with Boundary Elements **37**(3), 501–512 (2013)
26. Schanz, M.: A boundary element formulation in time domain for viscoelastic solids. Communications in Numerical Methods in Engineering **15**(11), 799–809 (1999)
27. Triantafyllidis, T.: 3-D time domain BEM using half-space Green's functions. Engineering Analysis with Boundary Elements **8**(3), 115–124 (1991)
28. Wolf, J.P: Dynamic soil-structure interaction. Prentice Hall, Englewood Cliffs (1985)
29. Zienkiewicz, O.C, Taylor, R.L.: The Finite Element Method, Volume I: The Basis. McGraw-Hill, New York (1967)